Asian Journal of Chemistry; Vol. 38, No. 3 (2026), 736-746
ASIAN JOURNAL OF CHEMISTRY
https://doi.org/10.14233/ajchem.2026.35338

Influence of Calcium Doping on the Structural, Vibrational and Optical Properties of Nickel Ferrite

PUNAM B. DUBE[1,*], YOGESH P. UABLE[2], TUKARAM SARAF[3], DILIP GARUD[4] and K.M. JADHAV[5]

[1]Department of Physics, Shri Madhavrao Patil Mahavidyalaya, Murum, Dharashiv-413605, India
[2]Department of Physics, Dr. Babasaheb Ambedkar Marathwada University, Chhatrapati Sambhajinagar-431004, India
[3]Twaritapuri Arts, Commerce and Science College, Talwada, Georai, Beed-431127, India
[4]Department of Physics, Adarsh College Omerga, Dharashiv-413606, India
[5]School of Basic and Applied Sciences, MGM University, Chhatrapati Sambhajinagr-431001, India

*Corresponding author: E-mail: punamdube188@gmail.com

Received: 26 November 2025 *Accepted*: 27 January 2026 *Published online*: 6 March 2026 AJC-22293

Calcium-doped nickel ferrite ($Ni_{1-x}Ca_xFe_2O_4$, x = 0.00, 0.05, 0.10, 0.15, 0.20) nanoparticles were synthesised using citric acid assisted sol-gel auto combustion method. X-ray diffraction (XRD) analysis confirmed the formation of a cubic spinel structure with single phase. Crystallite size obtained from Scherrer equation is in the range of 21 to 16 nm. An increase in lattice constant from 8.336 to 8.353Å with calcium doping is observed. FTIR spectra indicated typical metal-oxygen bond vibrations with absorption band located near at 600-400 cm^{-1}. Raman spectra revealed significant changes in vibrational modes ($T_{2g}(1)$, E_g, $T_{2g}(2)$, $T_{2g}(3)$ and $A_{1g}(1)$) due to the calcium doping. Morphological studies using SEM displayed a uniform grain growth with small agglomeration of nanoparticles. Grain size calculated from intercept method was 32.57 nm for bare nickel ferrite and 31.5 nm for Ca doped nickel ferrite (x = 0.10). TEM analysis revealed uniformly shaped nanoparticles, while the corresponding selected area electron diffraction (SAED) patterns confirmed the high crystallinity and phase purity of the synthesized samples. The optical absorption characteristics were examined using UV-Vis spectroscopy and Tauc plot analysis yielded band gap values between 1.74 and 1.78 eV. These findings demonstrate that calcium doping markedly influences the structural, vibrational, morphological and optical properties of nickel ferrite nanoparticles.

Keywords: Ca-doped nickel ferrite, Structural properties, Vibration modes, Optical properties.

INTRODUCTION

Nanotechnology has revolutionised material science by enabling the controlled synthesis of particles at the nanometer scale, imparting remarkable improvements in their physical, chemical and functional properties [1,2]. These properties of nanoparticles are different and superior compared to the bulk material. The precise tailoring of nanoparticle characteristics has uncovered new possibilities in electronics, medicines, catalysis and environmental remediation, presenting unprecedented opportunities for advanced applications [3,4]. Various methods such as bottom up approach and top down approach of nanotechnology have been used by several researchers to synthesize nanoparticles of different material [5]. Among various synthesis approaches, low-temperature and cost-effective wet chemical methods are widely employed by researchers, with the sol-gel auto-combustion technique being particularly favoured for the synthesis of ferrite nanoparticles [6].

Among various oxide materials, ferrites have attracted considerable attention due to their promising properties and wide range of technological applications. Ferrites can crystallize in different structural forms, including spinel, garnet, and hexagonal structures, among which spinel ferrites are particularly important because of their remarkable magnetic, electrical and catalytic properties [7,8]. Spinel ferrite nanoparticles generally follow the formula MFe_2O_4, where M represents divalent metal ions such as Zn^{2+}, Mg^{2+}, Cu^{2+}, Co^{2+} and Ni^{2+}. Owing to their chemical stability, biocompatibility, and tunable physico-chemical properties, spinel ferrite nanoparticles have been widely explored for applications in drug delivery, biomedical imaging, sensors and wastewater treatment [9,10].

Among spinel ferrites, nickel ferrite ($NiFe_2O_4$) is extensively studied due to its thermal, magnetic, electrical and chemical stability, along with tunable structural and optical properties [11-13]. Its inverse spinel structure, governed by cation distribution between tetrahedral (A) and octahedral (B) sites, allows property modification through cation substitution. Doping with divalent ions such as calcium introduces lattice distortions and alters physico-chemical and biocompatibility characteristics, enabling applications in catalysis, sensing, electronics and biomedical fields [14-16]. Also, synthesis conditions strongly influence ferrite properties and the sol-gel auto-combustion method using citric acid as a fuel is widely employed due to its ability to ensure homogeneous ion distribution, phase purity, and controlled nanoparticle morphology at relatively low temperatures [17-20].

Following synthesis, the comprehensive characterization using XRD, FTIR, FE-SEM, TEM, UV-visible and Raman spectroscopy provides insight into the phase structure, bonding environment, morphology and the optical-vibrational behaviour of ferrite nanoparticles [21,22]. Calcium substitution in nickel ferrite has been widely reported to influence lattice parameters, crystallite size, morphology, and magnetic properties due to the preferential occupation of Ca^{2+} ions at octahedral sites, which alters cation distribution and spin interactions [23-25]. These modifications can also affect optical absorption, elastic behaviour and vibrational modes, thereby expanding the applicability of Ca-doped nickel ferrite in the biomedical, catalytic, sensing and environmental applications [26]. Despite these advances, detailed correlations between structural parameters, lattice dynamics and vibrational characteristics remain limited. Therefore, the present work focuses on systematic structural and vibrational analysis, including lattice constant, microstrain, dislocation density, interatomic distances, interionic angles, Raman vibrational modes and Debye temperature, to better understand dopant-induced modifications in nickel ferrite nanoparticles.

EXPERIMENTAL

Characterisation: All the samples of Ca-doped nickel ferrite nanoparticle were characterised using X-ray diffractometer (Bruker D-8 Advance system). The X-ray diffraction was recorded at room temperature and in the 2θ range of 20º to 80º using Cu*K*α radiation. FTIR spectrometer (Bruker; ALPHA-T), was used to record the spectra at room temperature in the range of 4000-350 cm^{-1}. Raman spectrum was recorded using a Jobin Yvon Horibra LABRAM-HR 800 model system within the frequency between 900-100 cm^{-1}. The emission from the field A Carl Zeiss (Sigma field 300) model imaging microscope equipped with a sealed chamber was used to record scanning electron micrographs (FE-SEM) and energy dispersive X-ray (EDX) spectrum. The surface morphology was examined using a Joel/JEM 2100 PLUS transmission electron microscope (HR-TEM) model. UV-visible spectroscopy was used to evaluate the electronic band gap by recording absorption spectra at room temperature using a Perkin-Elmer Lambda-950 UV–Vis spectrophotometer.

Synthesis: Ca-doped nickel ferrites ($Ni_{1-x}Ca_xFe_2O_4$, x = 0.00, 0.05, 0.10, 0.15, 0.20) were synthesised using the sol-gel auto-combustion method. Separately, the solutions of ferric nitrate ($Fe(NO_3)_3 \cdot 9H_2O$), nickel nitrate ($Ni(NO_3)_2 \cdot 6H_2O$) and calcium nitrate ($Ca(NO_3)_3 \cdot 6H_2O$) were prepared in distilled water separately and then mixed together to obtain a homo-geneous mixed solution. Citric acid was added as a chelating agent in a 3:1 molar ratio (citric acid to total metal nitrates). The pH of the solution was adjusted to ~7 using ammonia solution, followed by continuous stirring and heating at 80 ºC until a viscous brown gel formed after solvent evaporation. The gel subsequently underwent spontaneous auto-combustion, obtaining a brown ash precursor. The obtained powder was then sintered at 650 ºC for 6 h to obtain Ca-doped $NiFe_2O_4$ nanoparticles.

RESULTS AND DISCUSSION

X-ray diffraction (XRD) studies: The structural characterisation of $Ni_{1-x}Ca_xFe_2O_4$ (x = 0.00, 0.05, 0.10, 0.15, 0.20) nanoparticles was performed using X-ray diffraction (XRD) method. The diffraction patterns (Fig. 1) with prominent peaks at 2θ values of 30.28º, 35.68º, 37.3º, 43.38º, 53.9º, 57.4º and 63.06º, which were indexed to the (220), (400), (422), (511), (440), (531) and (622) planes of the cubic spinel structure of nickel ferrite, consistent with JCPDS card no. 75-0894. The phase peaks confirms the formation of a single-phase Ca-doped nickel ferrite [9,27]. However, the XRD pattern also exhibits an appearance of secondary peak at 2θ = 33.20º, with less intensity is attributed to the Fe_2O_3 secondary phase. A similar reflection is reported in the JCPDS card no. 33-0664 [28]. Several researchers have also observed the presence of this Fe_2O_3 phase in their studies of $NiFe_2O_4$ ferrite with cation doping [29]. The origin of Fe_2O_3 secondary peaks in XRD is attributed to incomplete reaction or exceeding the solubility limit of dopants, which causes phase separation. If the amount of Ca^{2+} substituted for Ni^{2+} becomes too high or synthesis protocols (calcination temperature/time) are insufficient, some

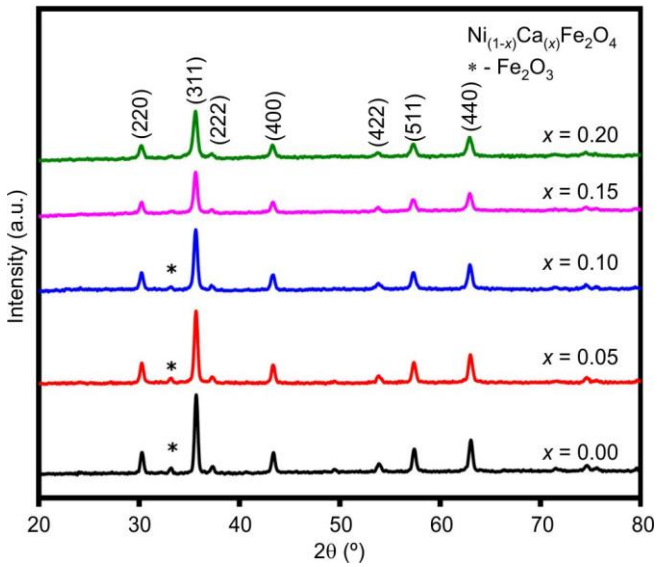

Fig. 1. XRD patterns of $Ni_{1-x}Ca_xFe_2O_4$ (x = 0.00, 0.05, 0.10, 0.15, 0.20) spinel ferrite nanoparticles

iron remains unreacted and crystallizes as α-Fe_2O_3, visible as secondary peaks in XRD [27]. The doping of Ca^{2+} ions having larger ionic radius (1.00 Å) in place of Ni^{2+} ions with lower ionic radii 0.56 Å leads to expansion of lattice. The highest intensity diffraction peaks observed nearby 35.66º Bragg's angle was used to calculate the crystallite size using the Scherrer formula [30].

$$D = \frac{k\lambda}{\beta \cos\theta} \quad (1)$$

where λ = 0.154 nm is the X-ray wavelength; θ is the Bragg angle; β is the full-width at half maximum (FWHM) of the diffraction peak and k = 0.9 is the shape factor. The values of crystallite size are presented in Table-1.

TABLE-1
VALUES OF LATTICE CONSTANT (a), X-RAY DENSITY (d_x), CRYSTALLITE SIZE (D) (by scherrer equation), d-SPACING (d) AND CRYSTALLITE SIZE (D by W-H) D_{W-H} FOR $Ni_{1-x}Ca_xFe_2O_4$ (x = 0.00, 0.05, 0.10, 0.15, 0.20) SPINEL FERRITE NANOPARTICLES

x	a (Å)	d_x (g/cm^3)	D (nm)	d (Å)	D_{W-H} (nm)
0.00	8.3366	5.3719	21	2.1453	32.24
0.05	8.3402	5.3435	22	2.4590	19.52
0.10	8.3474	5.3083	20	2.3428	21.59
0.15	8.3486	5.2849	19	2.7031	20.78
0.20	8.3534	5.2546	16	3.8463	19.09

Lattice constant (a) was calculated from the following equation [31].

$$a = d\sqrt{(h^2 + k^2 + l^2)} \quad (2)$$

where *hkl* represents the Miller indices of the crystal plane; and 'd' denotes the interplanar spacing.

The lattice constant values (Table-1) show increasing behaviour, which can be attributed to the fact that Ca^{2+} ion is having larger ionic radius as compared to Ni^{2+} ions. Usually, cations of larger ionic radii occupied octahedral site and leads to lattice expansion. Similar results are observed when cations of larger ionic radii replace the cations of lower ionic radii Ca^{2+} (1.00 Å) and Ni^{2+} ionic radii (0.56 Å) [32].

The unit cell volume was determined using the standard formula provided below.

$$V = a^3 \quad (3)$$

As the unit cell volume is directly related to the lattice constant, it exhibits an increasing trend consistent with that of the lattice constant [31]. Like lattice constant, unit cell volume also increases with Ca^{2+} doping. The ionic size differences between Ni^{2+} and Ca^{2+} induce lattice distortion causing a rise in the unit cell volume, consistent with Vegard's law.

The X-ray density (d_x) was calculated using eqn. 4:

$$d_x = \frac{ZM}{VN_A} \quad (4)$$

where Z is the coordination number (Z = 8) of cubic lattice; M is the molecular weight of the respective compositions; V is the unit cell volume and Avogadro's number (N_A = 6.022 × 10^{23}) [33]. Table-1 shows the calculated X-ray density values, which represents an increase with Ca^{2+} substitution due to the higher molecular weight of doped compositions [34].

The dislocation density (δ) values were calculated from the average crystallite size, using the following relationship between crystallite size and dislocation density [35,36].

$$\delta = \frac{1}{D^2} \quad (5)$$

Lattice strain (LS) is a microstructural parameter that indicates variations in lattice parameters caused by defects or dislocations within the crystal structure. It was determined using the following equation [37]:

$$LS = \frac{\beta}{4\tan\theta} \quad (6)$$

where θ denotes the angle at which the radiation is diffracted.

The microstrain (ε) was calculated using eqn. 7, while the stacking fault probability was determined using eqn. 8:

$$\varepsilon = \frac{\beta \cos\theta}{4} \quad (7)$$

$$SF = \frac{2\pi^2}{45}\sqrt{3}(\tan\theta) \quad (8)$$

The dislocation density (δ), lattice strain (LS) and stacking fault probability (SF) values for $Ni_{1-x}Fe_2Ca_xO_4$ (x = 0.00 to 0.20) nano-ferrites are presented in Table-2. As the Ca^{2+} concentration increases from 0.00 to 0.20, the dislocation density shows a steady rise from 2.30 × 10^{15} lines/m^2 to 4.45 × 10^{15} lines/m^2, indicating an increase in crystal defects due to lattice distortions induced by the dopant ions. Correspondingly, lattice strain also increases progressively, reaching a maximum value of 7.80 × 10^{-3} at the highest doping level, which reflects enhanced microstructural distortions and internal stresses within the spinel lattice. Notably, the stacking fault parameter remains relatively constant (~0.430) across all samples, suggesting that Ca^{2+} substitution predominantly influences dislocation density and strain rather than planar defects. The increase in dislocation density and strain is consistent with dopant induced lattice distortions and cation size mismatch effects, which disrupt the perfect crystal lattice and create more dislocations. These observations align well with reported trends in doped ferrite systems, where increased defect density and lattice strain are commonly observed with substitution doping, influencing the magnetic and mechanical properties of nanoferrites [38,39].

TABLE-2
VALUES OF UNIT CELL VOLUME (V), DISLOCATION DENSITY (δ), STACKING FAULT (SF), LATTICE STRAIN (LS) AND MICRO-STRAIN (ε) FOR $Ni_{1-x}Ca_xFe_2O_4$ (x = 0.00, 0.05, 0.10, 0.15, 0.20) SPINEL FERRITE NANOPARTICLES

x	V (Å)^3	$\delta \times 10^{14}$ (lines/m^2)	SF	LS × 10^{-4}	$\varepsilon \times 10^{-3}$
0.00	579.3	2.30	0.4305	5.61	5.61
0.05	580.1	2.46	0.4304	5.84	5.84
0.10	581.6	3.46	0.4303	6.89	6.89
0.15	581.8	3.56	0.4301	6.98	6.98
0.20	582.9	4.45	0.4301	7.80	7.80

The following formulae were applied to calculate the hopping distances, denoted as L_A and L_B [31].

$$L_A = a\sqrt{\frac{3}{4}} \quad (9)$$

$$L_B = a\sqrt{\frac{2}{4}} \quad (10)$$

The hopping lengths at the tetrahedral L_A and octahedral L_B sites, for $Ni_{1-x}Ca_xFe_2O_4$ (x = 0.00 to 0.20) nanoferrites, were calculated and the results are summarised in Table-3. Both L_A and L_B show a gradual increase with increasing Ca^{2+} concentration (from 3.610 Å to 3.617 Å for L_A and from 2.948 Å to 2.953 Å for L_B), indicating a slight expansion in the distance between neighboring magnetic ions. Such variations in hopping lengths and ionic radii are fundamental to understanding the magnetic behaviour and cation distribution in doped ferrites [40]. Table-3 shows the interstitial lattice sites at the tetrahedral and octahedral positions (r_A and r_B), calculated using the following equations [41]:

$$r_A = \left(u - \frac{1}{4}\right)a\sqrt{3} - r(O^{2-}) \quad (11)$$

$$r_B = \left(\frac{5}{8} - u\right)a - r(O^{2-}) \quad (12)$$

TABLE-3
VALUES OF HOPPING LENGTHS (L_A AND L_B), INTERSTITIAL RADII (r_A AND r_B) FOR $Ni_{1-x}Ca_xFe_2O_4$ (x = 0.00, 0.05, 0.10, 0.15, 0.20) SPINEL FERRITE NANOPARTICLES

x	L_A (Å)	L_B (Å)	r_A (Å)	r_B (Å)
0.00	3.0698	2.9474	0.47713	0.6424
0.05	3.6114	2.9487	0.47793	0.6433
0.10	3.6145	2.9512	0.4795	0.6451
0.15	3.6150	2.9516	0.4798	0.6454
0.20	3.6171	2.9533	0.4809	0.6465

Table-3 presents the interstitial radii values (r_A for tetrahedral sites and r_B for octahedral sites) for $Ni_{1-x}Ca_xFe_2O_4$ nanoparticles as the Ca^{2+} content increases. Both r_A and r_B show a gradual rise with increasing Ca^{2+} substitution as x increases from 0.00 to 0.20. This increasing value suggests that introducing Ca^{2+} ions, which possess a larger ionic radius than Ni^{2+}, leads to subtle lattice expansion and greater cation-cation spacing within the spinel.

The bond lengths at the tetrahedral and octahedral interstitial sites (d_{AX} and d_{BX}) were determined using eqn. 13 [42]:

$$d_{AX} = a\sqrt{3\left(u - \frac{1}{4}\right)} \quad (13)$$

$$d_{BX} = a\sqrt{3u^2 - \frac{11}{4}u + \frac{43}{64}} \quad (14)$$

where 'a' represent the lattice constant, while 'u' represents the positional parameter of oxygen.

The values for Tetraedge shared, Octaedge shared and unshared sites (d_{AXE}, d_{BXE} and d_{BEU}) were calculated using eqns. 15-17 [42]:

$$d_{AXE} = a\sqrt{2\left(2u - \frac{1}{2}\right)} \quad (15)$$

$$d_{BXE} = a\sqrt{2(1-2u)} \quad (16)$$

$$d_{BEU} = a\sqrt{4u^2 - 3u + \frac{11}{16}} \quad (17)$$

As shown in Table-4, the bond lengths at the tetrahedral, octahedral, shared and unshared octahedral sites increase with the substitution of Ca^{2+} ions at the Fe^{3+} octahedral positions. This leads to a slight lattice expansion due to the larger ionic radius of Ca^{2+} (1.00 Å) compared to Fe^{3+} (0.645 Å) [42].

TABLE-4
VALUES OF TETRAHEDRAL BOND LENGTH (d_{AX}), OCTAHEDRAL BOND LENGTH (d_{BX}), TETRAEDGE SHARED (d_{AXE}), OCTAEDGE SHARED (d_{BXE}) AND OCTAEDGE UNSHARED (d_{BEU}) FOR $Ni_{1-x}Ca_xFe_2O_4$ (x = 0.00, 0.05, 0.10, 0.15, 0.20) SPINEL FERRITE NANOPARTICLES

x	d_{AX} (Å)	d_{BX} (Å)	d_{AXE} (Å)	d_{BXE} (Å)	d_{BEU} (Å)
0.00	1.8771	2.0433	3.0653	2.8295	2.9486
0.05	1.8779	2.0442	3.0666	2.8307	2.9498
0.10	1.8795	2.0459	3.0693	2.8332	2.9524
0.15	1.8798	2.0462	3.0697	2.8336	2.9528
0.20	1.8809	2.0474	3.0715	2.8352	2.9545

The interatomic distances between metal cations and oxygen anions were calculated using established crystallographic equations. These distances include cation-cation separations (b, c, d, e and f) and cation-oxygen separations (p, q, r and s) [43,44].

The computational approach employs standard geometric relationships derived from the spinel crystal structure to determine these critical structural parameters [45], as shown in Tables 5 and 6:

TABLE-5
VALUES OF INTERIONIC DISTANCES (p, q, r, s) FOR $Ni_{1-x}Ca_xFe_2O_4$ (x = 0.00, 0.05, 0.10, 0.15, 0.20) SPINEL FERRITE NANOPARTICLE

x	p (Å)	q (Å)	r (Å)	s (Å)
0.00	2.0424	1.8771	3.5944	3.6339
0.05	2.0433	1.8779	3.5959	3.6354
0.10	2.0451	1.8795	3.5991	3.6386
0.15	2.0454	1.8798	3.5996	3.6391
0.20	2.0465	1.8809	3.6016	3.6412

TABLE-6
VALUES OF INTERIONIC DISTANCES (b, c, d, e, f) $Ni_{1-x}Ca_xFe_2O_4$ (x = 0.00, 0.05, 0.10, 0.15, 0.20) SPINEL FERRITE NANOPARTICLES

x	b (Å)	c (Å)	d (Å)	e (Å)	f (Å)
0.00	2.9474	3.4561	3.6098	5.4148	5.1051
0.05	2.9487	3.4576	3.6114	5.4171	5.1073
0.10	2.9512	3.4606	3.6145	5.4218	5.1111
0.15	2.9516	3.4611	3.6150	5.4225	5.1124
0.20	2.9533	3.4631	3.6171	5.4257	5.1154

$$P = a\left(\frac{5}{8} - u\right) \quad (18)$$

$$q = a\sqrt{3}\left(u - \frac{1}{4}\right) \quad (19)$$

$$r = a\sqrt{11}\left(u - \frac{1}{4}\right) \quad (20)$$

$$s = a\sqrt{3}\left(\frac{u}{3} + \frac{1}{8}\right) \quad (21)$$

$$b = \sqrt{2}\left(\frac{a}{4}\right) \quad (22)$$

$$2c = \sqrt{11}\left(\frac{a}{8}\right) \quad (23)$$

$$d = \sqrt{3}\left(\frac{a}{4}\right) \quad (24)$$

$$e = \sqrt{3}\left(\frac{3a}{8}\right) \quad (25)$$

$$f = \sqrt{6}\left(\frac{a}{4}\right) \quad (26)$$

The lattice constant (a) and interionic distances within $Ni_{1-x}Fe_2Ca_xO_4$ nanoferrites were systematically analysed to understand the effect of Ca^{2+}substitution on the spinel structure. As presented in Tables 5 and 6, the lattice parameter exhibits a slight but consistent increase from 8.339 Å to 8.355 Å as Ca^{2+} concentration increases from x = 0.00 to 0.20. This expansion is attributable to the larger ionic radius of Ca^{2+} compared to Ni^{2+}, which induces stretching of the unit cell and alters cationic arrangements. Correspondingly, the calculated interionic distances between the metal cations and oxygen anions, represented as p, q, r and s, show incremental increases, with p ranging from 2.043 Å to 2.046 Å and similar trends for q, r and s. These changes highlight a minor elongation in metal-oxygen bonds and interatomic separations. Likewise, the inter-cation distances (b, c, d, e and f) also gradually increase with Ca^{2+} doping, consistent with the expanded lattice framework, which influences the electronic environment and magnetic interactions within the ferrite. Such variations in lattice parameters and interionic distances have been reported previously in Ni^{2+}-based doped ferrite systems, confirming that ionic substitution at octahedral sites can effectively tailor the crystal structure and related physical properties [46].

Interionic angles: The bond angle measurements, represented as (θ_1, θ_2, θ_3, θ_4 and θ_5) were calculated using specific geometric relations based on the interionic distances, as summarised in Table-7.

TABLE-7
VALUES OF BOND ANGLES (θ_1, θ_2, θ_3, θ_4 and θ_5) FOR $Ni_{1-x}Ca_xFe_2O_4$ (x = 0.00, 0.05, 0.10, 0.15, 0.20) SPINEL FERRITE NANOPARTICLES

x	θ_1 (°)	θ_2 (°)	θ_3 (°)	θ_4 (°)	θ_5 (°)
0.00	123.66	146.40	92.37	125.81	75.35
0.05	123.66	146.40	92.37	125.81	75.35
0.10	123.66	146.39	92.36	125.78	75.35
0.15	123.66	146.38	92.36	125.81	75.35
0.20	123.84	146.63	92.55	125.94	75.53

$$\theta_1 = \cos^{-1}\left(\frac{p^2 + q^2 - c^2}{2pq}\right) \quad (27)$$

$$\theta_2 = \cos^{-1}\left(\frac{p^2 + r^2 - e^2}{2pr}\right) \quad (28)$$

$$\theta_3 = \cos^{-1}\left(\frac{2p^2 - b^2}{2p^2}\right) \quad (29)$$

$$\theta_4 = \cos^{-1}\left(\frac{p^2 + s^2 - f^2}{2ps}\right) \quad (30)$$

$$\theta_5 = \cos^{-1}\left(\frac{r^2 + q^2 - d^2}{2rq}\right) \quad (31)$$

The bond angles (θ_1-θ_5) for $Ni_{1-x}Fe_2Ca_xO_4$ (x = 0.00-0.20) nanoferrites are presented in Table-7, indicate slight structural changes when Ca^{2+} substitution. These small variations influence interatomic interactions within the lattice and may affect the magnetic and physical properties of the material. Taken together, the bond angles remain nearly stable, indicating preservation of the fundamental spinel structure, although minor lattice distortions occur due to Ca^{2+} substitution. Such behaviour is typical in doped spinel ferrites, where partial cation replacement causes slight shifts in atomic positions without altering the overall crystal framework. These minor structural changes are responsible for the variations in physicochemical properties of calcium-doped ferrites [47,48].

Williamson-Hall Plot (W-H plot): The microstrain was evaluated using the Williamson-Hall (W-H) approach, which accounts for XRD peak broadening contributions from both crystallite size and lattice strain [49]. According to this method, the relation between peak broadening and diffraction angle can be expressed as eqn. 32:

$$\beta\cos\theta = K\lambda D_{W-H} + 4\varepsilon\sin\theta \quad (32)$$

The crystallite size estimated from the W-H plots is shown in Table-1, while the corresponding lattice strain values are provided in Table-2. Furthermore, applying eqn. 1, the crystallite size was determined from the intercept on the Y-axis of the W-H plot and the obtained values showed good agreement with those calculated using the Scherrer equation [50]. The Williamson-Hall (W-H) plot method, which accounts for crystallite size and lattice strain, yielded slightly smaller sizes from 19 to 32 nm (Fig. 2), indicating the presence of microstrain induced by doping. The strain and microstrain values also increased with calcium content, suggesting enhanced lattice distortion and defects in the crystal structure.

FTIR studies: The infrared spectra of $Ni_{1-x}Ca_xFe_2O_4$ (x = 0.00, 0.05, 0.10, 0.15, 0.20) nanoferrites reveal two main absorption bands (533-562 cm^{-1}) attributed to tetrahedral metal-oxygen stretching (ν_1) and another between 424-383 cm^{-1} corresponding to octahedral site vibrations (ν_2). The higher frequency band at tetrahedral sites arises due to shorter Fe-O bonds and stronger force constants compared to octahedral sites [21,51]. From Fig. 3, it is observed that calcium doping has a marked influence on the vibrational wavenumbers. At lower Ca^{2+} concentrations (x = 0.05), both ν_1 and ν_2 slightly increase, reflecting enhanced lattice stiffness and cation rearr-

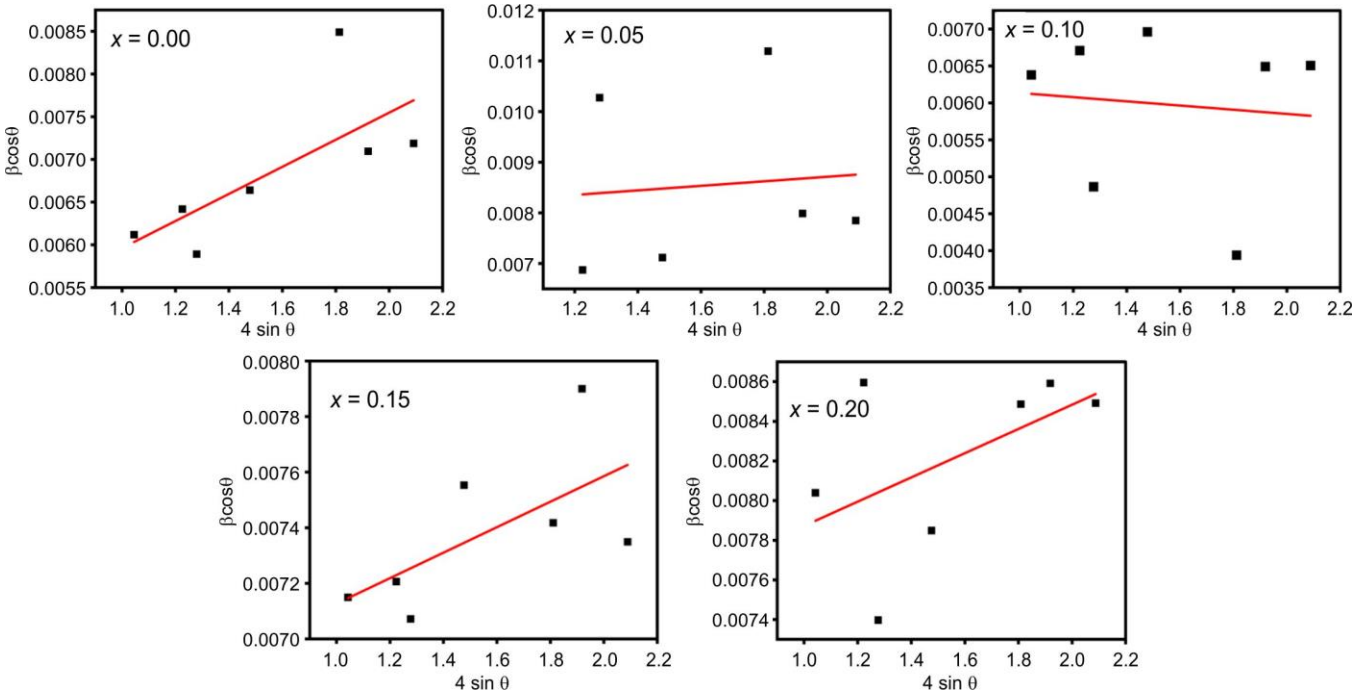

Fig. 2. W-H plot $Ni_{1-x}Ca_xFe_2O_4$ (x = 0.00, 0.05, 0.10, 0.15, 0.20) spinel ferrite nanoparticles

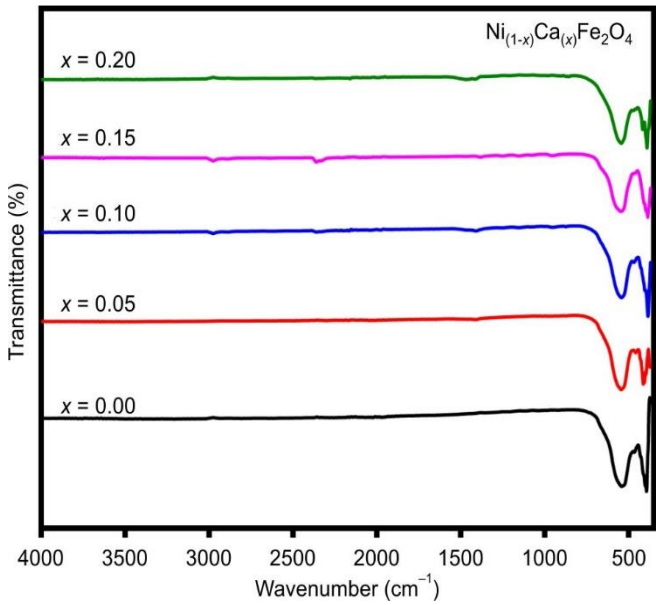

Fig. 3. FTIR spectra of $Ni_{(1-x)}Ca_xFe_2O_4$ (x = 0.00, 0.05, 0.10, 0.15, 0.20) spinel ferrite nanoparticles

angement, whereas at x = 0.10 and above, the bands shift further, indicating modified force constants due to substitution effects. Such nonlinear shifts are typical in doped ferrites, as the ionic radius and charge of Ca^{2+} disrupt the cation distribution and local bonding environment. These two frequencies of vibration, denoted as ν_1 and ν_2, correspond to the stretching vibrations in the tetrahedral (A) and octahedral (B) positions sublattices, correspondingly. The specific measurement of ν_1 and ν_2 is listed in Table-8, it is evident such both ν_1 and ν_2 increased and shifted to higher frequencies as Ca^{2+} ions are substituted into the system as according to Waldron's study [52].

TABLE-8
VALUES OF WAVENUMBER AT TETRAHEDRAL SITE (ν_1), WAVENUMBER AT OCTAHEDRAL SITE (ν_2), WAVENUMBER AVERAGE (ν_{avg}) AND DEBYE TEMPERATURE (θ_D) FOR $Ni_{1-x}Ca_xFe_2O_4$ (x = 0.00, 0.05, 0.10, 0.15, 0.20) SPINEL FERRITE NANOPARTICLE

x	ν_1 (cm^{-1})	ν_2 (cm^{-1})	ν_{avg} (cm^{-1})	θ_D (K)
0.00	544	397	470.5	677.43
0.05	545	415	480.0	691.11
0.10	536	394	465.0	669.51
0.15	533	424	478.5	688.95
0.20	562	383	475.5	684.63

The Debye temperature (θ_D) is also an essential physical constant that reflects the highest vibrational frequency attainable within a crystal lattice and provides an indication of the strength of interatomic bonding [31]:

$$\theta_D = \frac{hc\nu_{ave}}{K_B} \quad (33)$$

here, ν_{ave} denotes the average wavenumber of absorption, h is Plank's constant, c represents the speed of light and K_B stands for Boltzmann's constant.

The average vibrational frequency changes systematically and the calculated Debye temperature (θ_D) varies from 669 K to 691 K across the series. Higher θ_D values at x = 0.05 and 0.15 suggest increased lattice rigidity, a trend attributed to the combined effect of Ca^{2+} incorporation and the rearrangement of Fe^{3+} among available lattice sites. These θ_D values values (Table-8) demonstrate the influence of site-specific cation occupancy on the vibrational and thermal properties of the material [53].

Raman spectroscopy: In this study, the effect of Ca^{2+} doping on the Raman spectra of nickel ferrite was investigated. Changes in Raman peak positions are observed with

increasing Ca^{2+} content in $Ni_{1-x}Ca_xFe_2O_4$ nanoparticles (x = 0.00, 0.05, 0.10, 0.15, 0.20). The Ca^{2+}-doped nickel ferrite adopts an inverse spinel structure and shows five main Raman modes *viz*., $T_{2g}(1)$, E_g, $T_{2g}(2)$, $T_{2g}(3)$ and $A_{1g}(1)$ (Fig. 4) [9] and the Raman shift values for various Ca^{2+} doping levels are shown in Table-9. These Raman modes illustrates the evolution of these Raman peaks with increasing Ca^{2+} content, highlighting variations in peak intensity and position. This behaviour reflects the impact of Ca^{2+} doping on the vibrational properties of the ferrite structure [54]. The gradual change in peak positions suggests an increase in lattice strain and variation in bond lengths caused by the larger ionic radius of Ca^{2+} compared to Ni^{2+}. Thus, the Raman analysis confirms that Ca^{2+} doping modifies the structure in nickel nanoferrites,

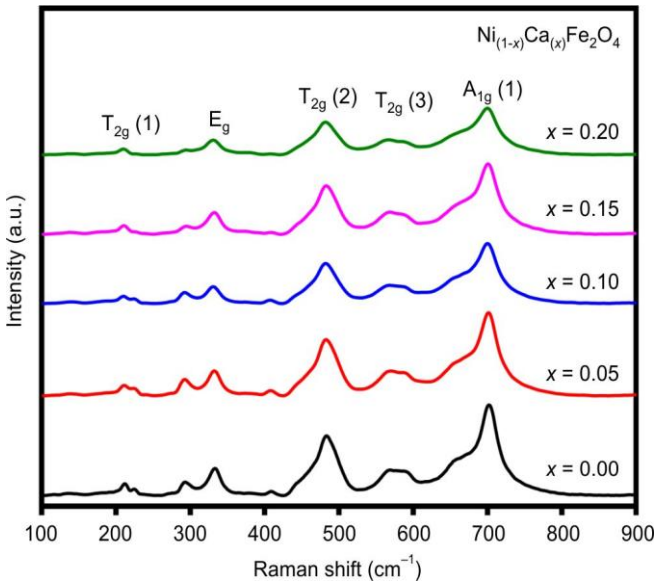

Fig. 4. Raman spectra of $Ni_{1-x}Ca_xFe_2O_4$ (x = 0.00, 0.05, 0.10, 0.15, 0.20) spinel ferrite nanoparticles

TABLE-9
RAMAN MODE LABELS FOR $Ni_{1-x}Ca_xFe_2O_4$ (x = 0.00, 0.05, 0.10, 0.15, 0.20) SPINEL FERRITE NANOPARTICLES

x	$T_{2g}(1)$ (cm^{-1})	E_g (cm^{-1})	$T_{2g}(2)$ (cm^{-1})	$T_{2g}(3)$ (cm^{-1})	$A_{1g}(1)$ (cm^{-1})
0.00	211.65	333.45	483.25	566.90	699.04
0.05	211.65	331.95	481.75	569.90	702.54
0.10	208.65	330.62	481.75	568.40	700.54
0.15	209.65	331.95	483.25	566.90	702.54
0.20	210.15	330.62	481.75	566.90	699.04

affecting the Fe-O bond lengths and cation distribution, which is consistent with minor lattice distortions and strain development seen in the samples.

FE-SEM studies: The morphology and microstructural characteristics of $Ni_{1-x}Ca_xFe_2O_4$ (x = 0.00 and 0.10) were investigated using FE-SEM as shown in Fig. 5a and 5d. The images reveal mostly spherical nanoparticles that tend to agglomerate in localised regions. Figs. 5b and 5e show the histogram of the grain size was measured at approximately for undoped sample 32.5 nm, for doped sample 31.5 nm confirming the nanocrystalline nature of the samples. FE-SEM results also suggest that grain growth occurs gradually but unevenly. At lower Ca^{2+} concentrations, the incorporation of Ca^{2+} ion enhances pore mobility by creating additional cation vacancies, which influences the microstructure of nickel ferrite. Grain size analysis for all compositions was performed using ImageJ software [55].

The EDX spectra (Figs. 5c and 5f) confirm the presence of Ni, Fe, Ca, and O elements, with compositions closely matching the expected stoichiometric ratios. The corresponding atomic and weight percentages show good agreement between the experimental and calculated values. Furthermore, elemental mapping analysis demonstrates the uniform distribution of these elements throughout the nanoparticles.

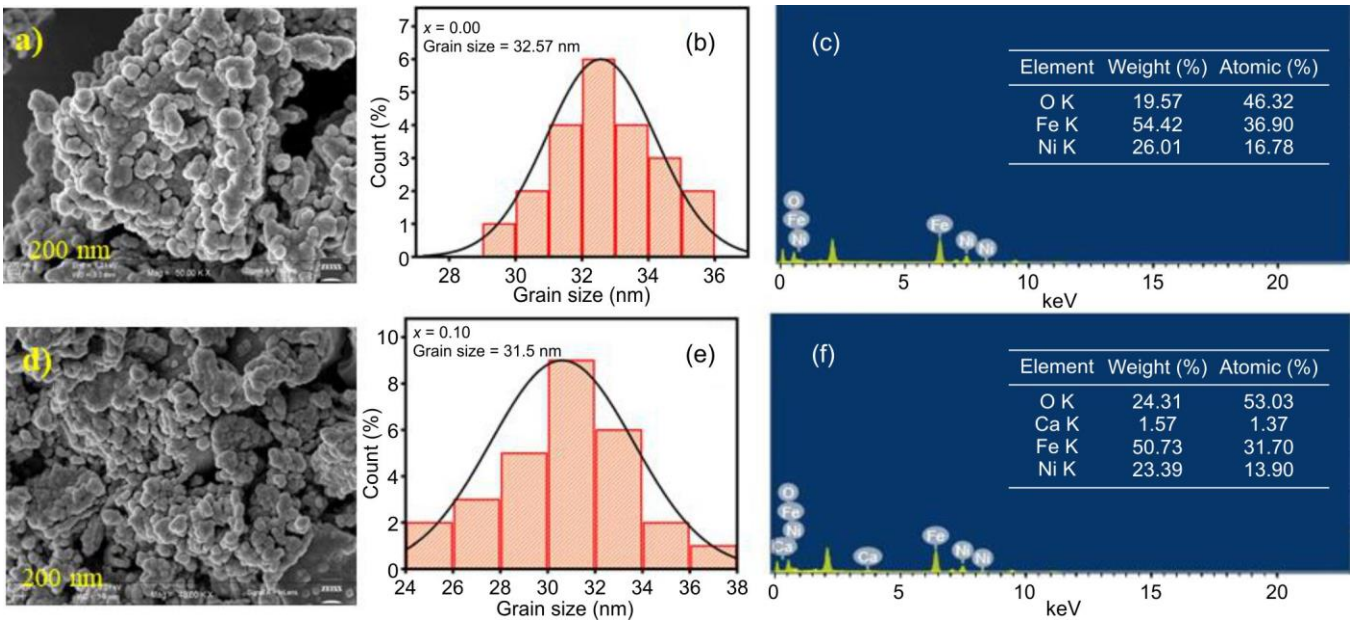

Fig. 5. FE-SEM images (a and d) with histogram (b and e) and EDX spectra (c and f) of $Ni_{1-x}Ca_xFe_2O_4$ (x = 0.00 and 0.10) spinel ferrite nanoparticles

HRTEM studies: The HRTEM analysis verified that the prepared $Ni_{1-x}Ca_xFe_2O_4$ (x = 0.05, 0.20) nanoferrites consist of nearly spherical nanoparticles exhibiting slight agglomeration, mainly due to the magnetic interactions. The HRTEM images (Fig. 6) confirm these morphological observations. The corresponding SAED patterns (Fig. 6) show distinct concentric rings. The interplanar spacing calculated from the ring diameters correspond well to the (111), (220), (311), (222), (400), (422) and (511) crystal planes of $NiFe_2O_4$, consistent with the planes identified in the XRD patterns. These findings confirm the formation of a crystalline spinel phase.

UV-Visible spectroscopy: For UV-Vis measurements, dispersed powder samples of $Ni_{1-x}Ca_xFe_2O_4$ (x = 0.00, 0.05, 0.10, 0.15, 0.20) were prepared in distilled water using a cuvette. The UV-visible absorption spectra of Ca^{2+}-doped nickel ferrite were recorded over the wavelength range of 200-800 nm for different doping concentrations, as shown in Fig. 7. The undoped sample shows low absorption with a gradual rise at shorter wavelengths. As Ca^{2+} concentration increases, the absorption intensity systematically raises, particularly in the 350-600 nm regions, with a noticeable red shift. The increasing peak intensity confirms effective doping and alteration of the electronic structure. The smooth absorption trend suggests uniform Ca^{2+} distribution, making these materials promising for photocatalytic and optoelectronic applications that require strong UV-visible light absorption [56].

The optical band gap (E_g) of Ca^{2+}-doped nanoferrite samples was determined using Tauc plots (Fig. 8) and the Kubelka-Munk function. The band gap energies were calculated from the Tauc equation:

$$(\alpha h\nu)^n = A(h\nu - E_g) \quad (34)$$

where α is the absorption coefficient, $h\nu$ represent the photon energy; A is a proportionality constant, E_g indicates the optical band gap and n is an index varies on type of the electronic transition and n is an index that depends on the type of electronic transition. For an indirect allowed transition, n equals 2, whereas for direct allowed transitions, n is 1/2. In this work, n

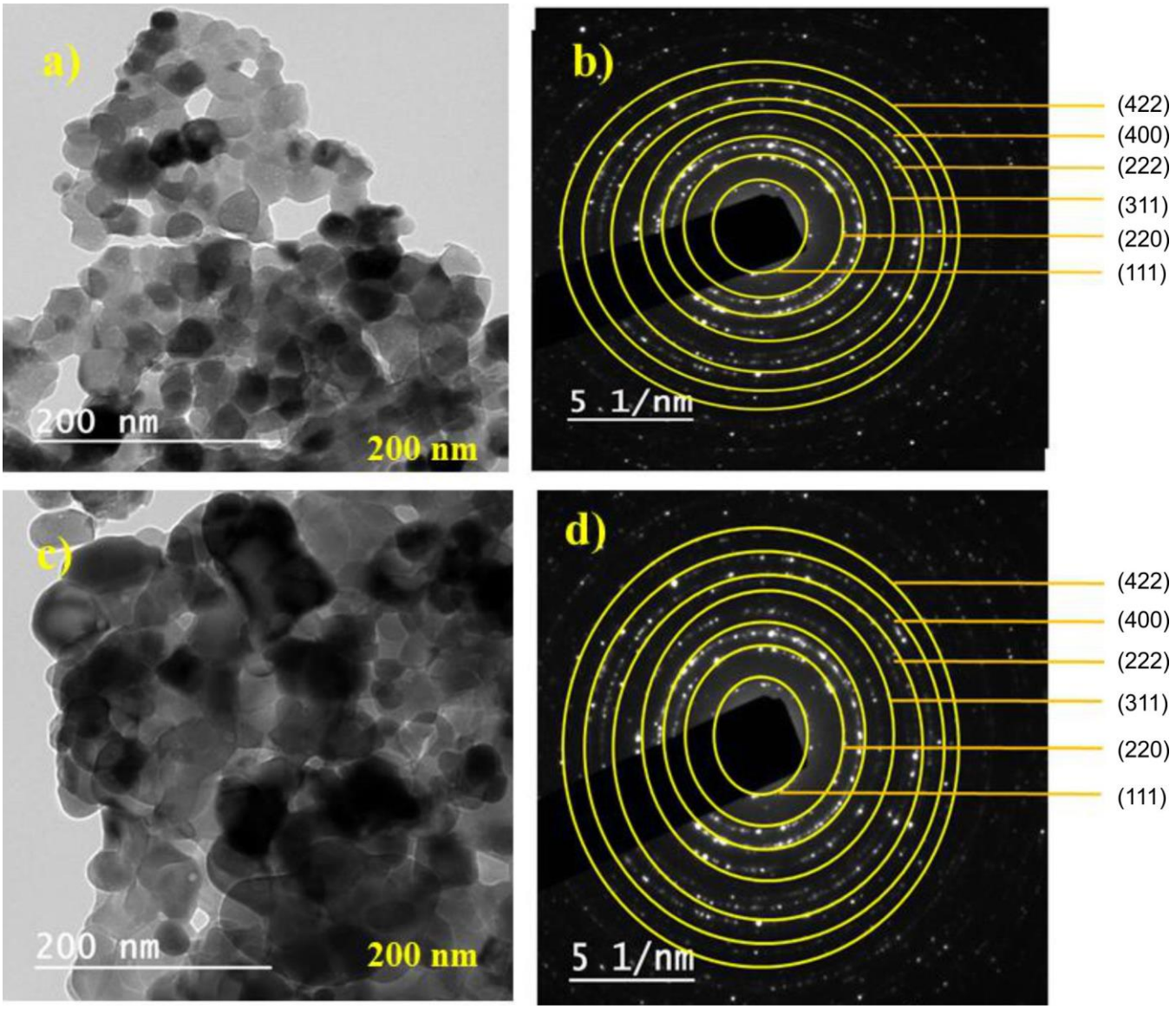

Fig. 6. HR-TEM images (a and c) and SAED (b and d) patterns of $Ni_{1-x}Ca_xFe_2O_4$ (x = 0.05 and 0.20) spinel ferrite nanoparticles

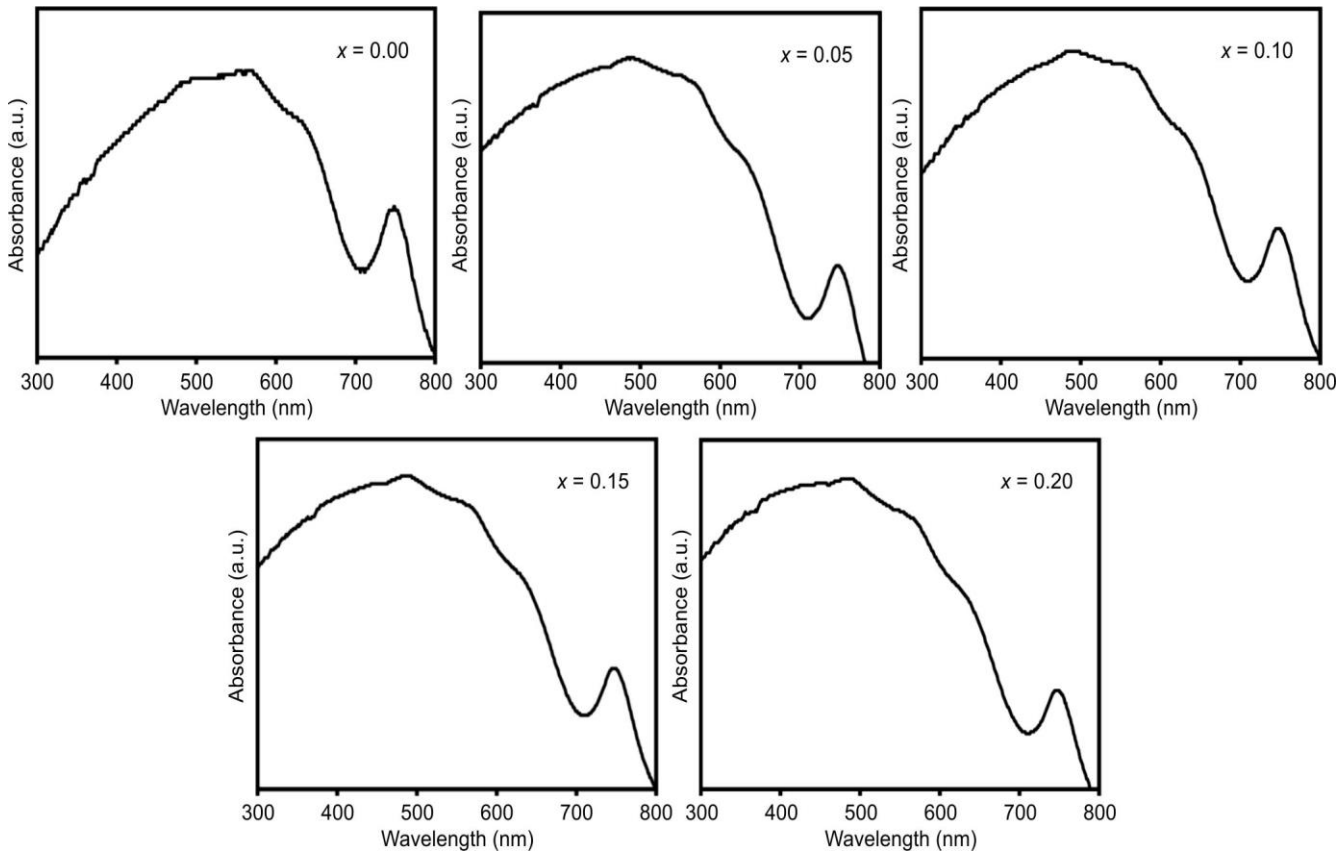

Fig. 7. UV-Vis absorbance spectra of $Ni_{1-x}Ca_xFe_2O_4$ (x = 0.00, 0.05, 0.10, 0.15, 0.20) spinel ferrite nanoparticles

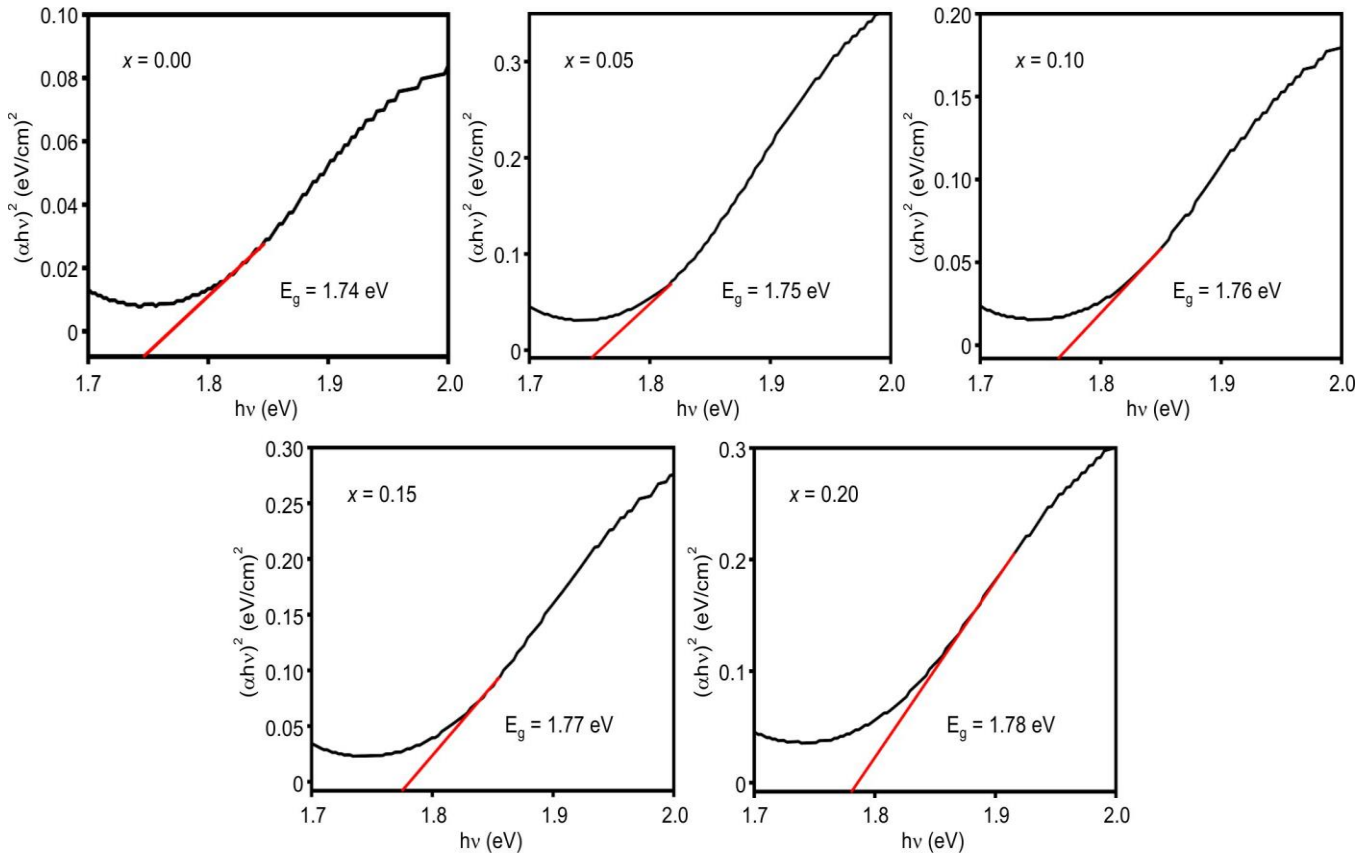

Fig. 8. Tauc's plot for the energy band gap of $Ni_{1-x}Ca_xFe_2O_4$ (x = 0.00, 0.05, 0.10, 0.15, 0.20) spinel ferrite nanoparticles

is taken as 2, corresponding to indirect allowed transitions. The positive slope observed in the plot confirms the direct nature of the electronic transitions. Band gap values were obtained by extrapolating the linear portion of the $(\alpha h\nu)^2$ *versus* $h\nu$ plot to the *x*-axis [57].

The values of optical band gap (Table-10), a gradual increase in band gap energy was observed with rising Ca^{2+} concentration. This trend can be attributed to the Burstein-Moss effect, where an increase in carrier concentration causes the Fermi level to shift into the conduction band. The substitution of Fe^{3+} ions (0.67 Å) by larger Ca^{2+} (1.00 Å) ions induces lattice strain, modifying the electronic band structure and potentially creating new energy levels within the band gap. The sharp absorption edge and smooth curves indicate good crystallinity and uniform dopant distribution, reflecting the high quality of the synthesised samples [14].

TABLE-10
BAND-GAP ENERGY (eV) DATA OF $Ni_{1-x}Ca_xFe_2O_4$ (x = 0.00, 0.05, 0.10, 0.15, 0.20) SPINEL FERRITE NANOPARTICLES

Composition (x)	0.00	0.05	0.10	0.15	0.20
Energy band-gap (eV)	1.74	1.75	1.76	1.77	1.78

Conclusion

The synthesised $Ni_{1-x}Ca_xFe_2O_4$ (x = 0.00, 0.05, 0.10, 0.15, 0.20) nanoferrites exhibit remarkable modifications in structural and physical characteristics with increasing Ca^{2+} content. XRD analysis confirmed the spinel cubic phase, with an average crystallite size decreasing from 21 nm to 16 nm upon Ca^{2+} doping, indicating crystallite refinement due to lattice strain. FTIR and Raman spectral analyses further validated metal-oxygen bonding and cation distribution changes. SEM and HR-TEM studies revealed well-dispersed nanoparticles with grain sizes ranging between 20 and 30 nm, consistent with XRD results. The UV-Vis spectra showed an increase in the optical band gap from about 1.74 eV to 1.78 eV as Ca^{2+} concentration increased, suggesting enhanced electronic interactions and altered surface states. The obtained experimental results on structural, infrared and optical study are found useful for photocatalytic application.

ACKNOWLEDGEMENTS

Punam B. Dube expresses thanks to the Institute of Chemical Technology Marathwada Campus in Jalna for providing the XRD facility. The Department of Chemistry at Dr. Babasaheb Ambedkar Marathwada University in Aurangabad is recognised for providing the FTIR service. Additionally, the Indian Institute of Technology, SAIF and Madras (IITM) is credited with delivering the VSM capability.

CONFLICT OF INTEREST

The authors declare that there is no conflict of interests regarding the publication of this article.

DECLARATION OF AI-ASSISTED TECHNOLOGIES

During the preparation of this manuscript, the authors used an AI-assisted tool(s) to improve the language. The authors reviewed and edited the content and take full responsibility for the published work.

REFERENCES

1. Y. Khan, H. Sadia, S.Z. Ali Shah, M.N. Khan, A.A. Shah, N. Ullah, M.F. Ullah, H. Bibi, O.T. Bafakeeh, N.B. Khedher, S.M. Eldin, B.M. Fadhl and M.I. Khan, *Catalysts*, **12**, 1386 (2022); https://doi.org/10.3390/catal12111386
2. J. Mehta, K. Pathania and S.V. Pawar, *Sustain. Food Technol.*, **3**, 947 (2025); https://doi.org/10.1039/D5FB00122F
3. P. Lakhani, D. Bhanderi and C.K. Modi, *J. Nanopart. Res.*, **26**, 148 (2024); https://doi.org/10.1007/s11051-024-06053-9
4. F.J. Tovar-Lopez, *Sensors*, **23**, 5406 (2023); https://doi.org/10.3390/s23125406
5. M.Z. Ul Abidin, M. Ikram, S. Moeen, G. Nazir, M.B. Kanoun and S. Goumri-Said, *Coord. Chem. Rev.*, **520**, 216158 (2024); https://doi.org/10.1016/j.ccr.2024.216158
6. S.G. Divakara and B. Mahesh, *Results Eng.*, **21**, 101702 (2024); https://doi.org/10.1016/j.rineng.2023.101702
7. S.J. Salih and W.M. Mahmood, *Heliyon*, **9**, e16601 (2023); https://doi.org/10.1016/j.heliyon.2023.e16601
8. F.G. Silva, J. Depeyrot, A.F.C. Campos, R. Aquino, D. Fiorani and D. Peddis, *J. Nanosci. Nanotechnol.*, **19**, 4888 (2019); https://doi.org/10.1166/jnn.2019.16877
9. S. Nawale, K. Deshmukh, K. Gurav, A. Keche and K.M. Jadhav, *AIP Conf. Proc.*, **3198**, 020024 (2025); https://doi.org/10.1063/5.0248448.
10. K.K. Deshmukh, S.P. Nawale, K.A. Gurav, S. Bhagat, A.P. Keche and K.M. Jadhav, *Ceram. Int.*, **51**, 38039 (2025); https://doi.org/10.1016/j.ceramint.2025.06.043
11. G. Rana, P. Dhiman, A. Kumar, D.-V.N. Vo, G. Sharma, S. Sharma, and M. Naushad, *Chem. Eng. Res. Design*, **175**, 182 (2021); https://doi.org/10.1016/j.cherd.2021.08.040
12. A.N. Nabeel, A. Jain, R. Kumar, S. Sharma, C. Li, S.P. Dwivedi, K.S. Naidu, S. Gupta, A. Kumar, M. Abbas and K.A. Mohammed, *Ionics*, **31**, 1233 (2025); https://doi.org/10.1007/s11581-024-05971-x
13. J. Patra and V.K. Verma, *Nano-Struct. Nano-Objects*, **42**, 101458 (2025); https://doi.org/10.1016/j.nanoso.2025.101458
14. Y.P. Ubale, P.S. Patil, S.S. Gawali, S.V. Rathod and K.M. Jadhav, *Appl. Phys., A Mater. Sci. Process.*, **131**, 237 (2025); https://doi.org/10.1007/s00339-025-08383-4
15. Y.P. Ubale, P.S. Patil, S.S. Gawali, S.K. Modi, K.B. Modi and K.M. Jadhav, *J. Supercond. Nov. Magn.*, **38**, 93 (2025); https://doi.org/10.1007/s10948-025-06935-6
16. Y.P. Ubale, P.S. Patil; S.S. Gawali and K.M. Jadhav, *AIP Conf. Proc.*, **3198**, 020016 (2025); https://doi.org/10.1063/5.0248343
17. S. Bhattacharya and S.K. Samanta, *Chem. Rev.*, **116**, 11967 (2016); https://doi.org/10.1021/acs.chemrev.6b00221
18. M. Arif, H. Raza and T. Akhter, *RSC Adv.*, **14**, 24604 (2024); https://doi.org/10.1039/D4RA04128C
19. T.J. Merkel, K.P. Herlihy, J. Nunes, R.M. Orgel, J.P. Rolland and J.M. DeSimone, *Langmuir*, **26**, 13086 (2010); https://doi.org/10.1021/la903890h
20. H.J. Kwon, K. Shin, M. Soh, H. Chang, J. Kim, J. Lee, G. Ko, B.H. Kim, D. Kim and T. Hyeon, *Adv. Mater.*, **30**, 1704290 (2018); https://doi.org/10.1002/adma.201704290
21. A.A. Nawpute, S.D. Tapsale, S.S. Gawali, S.P. More and K.M. Jadhav, *J. Electron. Mater.*, **53**, 2250 (2024); https://doi.org/10.1007/s11664-024-10971-8
22. P.G. Shinde, S.M. Wani, M.T. Kotkar, A.G. Patil and K.M. Jadhav, *J. Mater. Sci. Mater. Electron.*, **36**, 1566 (2025); https://doi.org/10.1007/s10854-025-15638-6

23. T. Vigneswari and P. Raji, *J. Mol. Struct.*, **1127**, 515 (2017); https://doi.org/10.1016/j.molstruc.2016.07.116
24. S. Gopale, M.R. Patil, R.M. Borade, J.M. Bhandari and K.M. Jadhav, *Adv. Mater. Res.*, **1169**, 79 (2022); https://doi.org/10.4028/p-95jpl8
25. R.G. Andrade, D. Ferreira, S.R.S. Veloso, C. Santos-Pereira, E.M.S. Castanheira, M. Côrte-Real and L.R. Rodrigues, *Pharmaceutics*, **14**, 2694 (2022); https://doi.org/10.3390/pharmaceutics14122694
26. S.S. Thomas, I.H. Joe, P. Aswathy, E. Mathew and A.A. Noble, *Mater. Sci. Eng. B*, **297**, 116696 (2023); https://doi.org/10.1016/j.mseb.2023.116696
27. P.R. Tiwari, R.P. Singh, K. Bharati, A.C. Yadav, B.C. Yadav, A. Singh, M.P. Singh and S. Kumar, *J. Dispers. Sci. Technol.*, **45**, 2155 (2024); https://doi.org/10.1080/01932691.2023.2256383
28. B.J. Rani, B. Saravanakumar, G. Ravi, V. Ganesh, S. Ravichandran and R. Yuvakkumar, *J. Mater. Sci. Mater. Electron.*, **36**, 1059 (2025); https://doi.org/10.1007/s10854-025-15093-3
29. K. Verma, N. Goyal, M. Singh, M. Singh and R.K. Kotnala, *Results Phys.*, **13**, 102212 (2019); https://doi.org/10.1016/j.rinp.2019.102212
30. S. Nasiri, M. Rabiei, A. Palevicius, G. Janusas, A. Vilkauskas, V. Nutalapati and A. Monshi, *Nano Trends*, **3**, 100015 (2023); https://doi.org/10.1016/j.nwnano.2023.100015
31. P.S. Patil, Y.P. Ubale, S.S. Gawali, M.R. Pai and K.M. Jadhav, *Ceram. Int.*, **50**, 54155 (2024); https://doi.org/10.1016/j.ceramint.2024.10.272
32. R.K. Singh, M. Srivastava, N.K. Prasad and S. Kannan, *J. Alloys Compd.*, **725**, 393 (2017); https://doi.org/10.1016/j.jallcom.2017.07.113
33. L. Glasser, *J. Chem. Educ.*, **88**, 581 (2011); https://doi.org/10.1021/ed900046k
34. M.T. Kotkar, S.M. Wani, P.G. Shinde, A.G. Patil and K.M. Jadhav, *Solid State Commun.*, **400**, 115914 (2025); https://doi.org/10.1016/j.ssc.2025.115914
35. K. Venkateswarlu, M. Sandhyarani, T.A. Nellaippan and N. Rameshbabu, *Proc. Mater. Sci.*, **5**, 212 (2014); https://doi.org/10.1016/j.mspro.2014.07.260
36. N. Kumar, B. Roy and J. Das, *J. Alloys Compd.*, **618**, 139 (2015); https://doi.org/10.1016/j.jallcom.2014.08.131
37. J. Gubicza, L. Balogh, R.J. Hellmig, Y. Estrin and T. Ungár, *Mater. Sci. Eng. A*, **400-401**, 334 (2005); https://doi.org/10.1016/j.msea.2005.03.042
38. B.V. Prasad, B.R. Babu and M.S.R. Prasad, *Mater. Sci. Pol.*, **33**, 806 (2015); https://doi.org/10.1515/msp-2015-0111
39. R. UmashankaraRaja, Y.S. Vidya, H.C. Manjunatha, M. Priyanka, R. Munirathnam, K.M. Rajashekara, S. Manjunatha and E. Krishnakanth, *Green Energy Resour.*, **2**, 100059 (2024); https://doi.org/10.1016/j.gerr.2024.100059
40. O. Hemeda and M. Barakat, *J. Magn. Magn. Mater.*, **223**, 127 (2001); https://doi.org/10.1016/S0304-8853(00)00521-7
41. Q. Zhu, G. Xiao, Y. Cui, W. Yang, S. Wu, G.-H. Cao and Z. Ren, *J. Alloys Compd.*, **878**, 160290 (2021); https://doi.org/10.1016/j.jallcom.2021.160290
42. M. Patil, M.K. Rendale, S.N. Mathad and R.B. Pujar, *Int. J. Self-Propag. High-Temp. Synth.*, **26**, 33 (2017); https://doi.org/10.3103/S1061386217010083
43. S. Shatooti and M. Mozaffari, *Sci. Rep.*, **14**, 12992 (2024); https://doi.org/10.1038/s41598-024-64016-5
44. K.V. Bab, G. Satyanarayana, B. Sailaja, G.V. Santosh Kumar, K. Jalaiah and M. Ravi, *Results Phys.*, **9**, 55 (2018); https://doi.org/10.1016/j.rinp.2018.01.048
45. P.S. Patil, M.V. Khedkar, Y.P. Ubale, S.S. Gawali and K.M. Jadhav, *J. Mater. Sci. Mater. Electron.*, **36**, 1014 (2025); https://doi.org/10.1007/s10854-025-15005-5
46. S.S. Wanjari, D.V. Nandanwar, K.G. Rewatkar and A.V. Gongal, *Nano-Struct. Nano-Objects*, **43**, 101540 (2025); https://doi.org/10.1016/j.nanoso.2025.101540
47. S.A. Jadhav, S.B. Somvanshi, S.S. Gawali, K. Zakde and K.M. Jadhav, *J. Rare Earths*, **42**, 488 (2024); https://doi.org/10.1016/j.jre.2023.03.004
48. S.B. Somvanshi, S.A. Jadhav, S.S. Gawali, K. Zakde and K.M. Jadhav, *J. Alloys Compd.*, **947**, 169574 (2023); https://doi.org/10.1016/j.jallcom.2023.169574
49. S.A. Jadhav, S.B. Somvanshi, M.V. Khedkar, S.R. Patade and K.M. Jadhav, *J. Mater. Sci. Mater. Electron.*, **31**, 11352 (2020); https://doi.org/10.1007/s10854-020-03684-1
50. S.A. Jadhav, A.V. Raut, M.V. Khedkar, S.B. Somvanshi and K.M. Jadhav, *Adv. Mater. Res.*, **1169**, 123 (2022); https://doi.org/10.4028/p-f695kb
51. P.S. Patil, S. Bhagat, R. Kokate and K.M. Jadhav, *AIP Conf. Proc.*, **3198**, 020032 (2025); https://doi.org/10.1063/5.0248275
52. R. Waldron, *Phys. Rev.*, **99**, 1727 (1955); https://doi.org/10.1103/PhysRev.99.1727
53. V.K. Mande, J.S. Kounsalye, S.K. Vyawahare and K.M. Jadhav, *J. Mater. Sci. Mater. Electron.*, **30**, 56 (2019); https://doi.org/10.1007/s10854-018-0252-1
54. W. Cochran, *CRC Crit. Rev. Solid State Sci.*, **2**, 1 (1971); https://doi.org/10.1080/10408437108243425
55. V.U. Magar, S.V. Rathod, P.S. Patil, S. More and M.K. Babrekar, *J. Mater. Sci. Mater. Electron.*, **35**, 967 (2024); https://doi.org/10.1007/s10854-024-12705-2
56. G. Rana, P. Dhiman, A. Kumar, E.A. Dawi and G. Sharma, *Chem. Phys. Impact*, **8**, 100507 (2024); https://doi.org/10.1016/j.chphi.2024.100507
57. S.V. Rathod, V.U. Magar, S.V. Rajmane, D.R. Sapate and K.M. Jadhav, *J. Mater. Sci. Mater. Electron.*, **36**, 191 (2025); https://doi.org/10.1007/s10854-025-14227-x